Young Black Hole and Neutron Star Systems in the Nearby Star-forming Galaxy M33: The NuSTAR View

Jun Yang[1] , Daniel R. Wik[2] , Bret D. Lehmer[3] , Lacey A. West[3] , Benjamin F. Williams[4] , Thomas J. Maccarone[5] ,
Andrew Ptak[6] , Mihoko Yukita[6,7] , Neven Vulic[6,8,9,10] , Dominic J. Walton[11,12] , Kristen Garofali[6] , and Vallia Antoniou[5]

[1] Department of Physics and Kavli Institute for Astrophysics and Space Research, Massachusetts Institute of Technology, One Kendall Square, Building 300 NE83-535, Cambridge, MA 02139, USA; yangjun@mit.edu
[2] Department of Physics & Astronomy, University of Utah, 115 S 1400 E, Salt Lake City, UT 84112-0830, USA
[3] Department of Physics, University of Arkansas, 226 Physics Building, 825 West Dickson Street, Fayetteville, AR 72701, USA
[4] Department of Astronomy, Box 351580, University of Washington, Seattle, WA 98195, USA
[5] Department of Physics and Astronomy, Texas Tech University, Box 41051, Lubbock, TX 79409-1051, USA
[6] Laboratory for X-Ray Astrophysics, Code 662, NASA Goddard Space Flight Center, Greenbelt, MD 20771, USA
[7] The Johns Hopkins University, Homewood Campus, Baltimore, MD 21218, USA
[8] Eureka Scientific, Inc., 2452 Delmer Street, Suite 100, Oakland, CA 94602-3017, USA
[9] Department of Astronomy, University of Maryland, College Park, MD 20742-2421, USA
[10] Center for Research and Exploration in Space Science and Technology, NASA/GSFC, Greenbelt, MD 20771, USA
[11] Centre for Astrophysics Research, University of Hertfordshire, College Lane, Hatfield AL10 9AB, UK
[12] Institute of Astronomy, University of Cambridge, Madingley Road, Cambridge CB3 0HA, UK
Received 2021 October 29; revised 2022 March 2; accepted 2022 March 23; published 2022 May 4

Abstract

We can learn about the formation and evolution of compact objects, such as neutron stars and black holes (BHs), by studying the X-ray emission from accreting systems in nearby star-forming galaxies. The hard ($E > 10$ keV) X-ray emission in particular allows strong discrimination among the accretion states and compact object types. We conducted a NuSTAR survey ($\sim$600 ks) of the Local Group spiral galaxy M33 to study the distribution of X-ray binary (XRB) accretors in an actively star-forming environment. We constructed color–intensity and color–color diagrams to infer XRB accretion states. Using these diagrams, we have classified 28 X-ray sources in M33 by comparing their hard X-ray colors to those of known systems. Four sources lie in the parameter space occupied by X-ray pulsars, while 8, 10, and 4 sources lie in the parameter space occupied by BHs in the hard, intermediate, and soft states, respectively. The known ultraluminous X-ray source M33 X-8 is also found to be consistent with that source type. Some sources overlap within the Z/Atoll sources due to the overlap of the two categories of BHs and Z/Atoll sources. In contrast to a similar NuSTAR survey of M31 (with a low-mass XRB-dominant population), the source population in M33 is dominated by high-mass XRBs (HMXBs), allowing the study of a very different population with similar sensitivity due to the galaxy's similar distance. This characterization of a population of HMXB accretion states will provide valuable constraints for theoretical XRB population synthesis studies to their formation and evolution.

Unified Astronomy Thesaurus concepts: Neutron stars (1108); Compact objects (288); Black holes (162); Triangulum Galaxy (1712); Accretion (14); Stellar accretion (1578); Classification (1907); Ultraluminous x-ray sources (2164); High mass x-ray binary stars (733); X-ray binary stars (1811); Stellar classification (1589)

1. Introduction

The X-ray binaries (XRBs) probe the late stages of evolution of mass-exchanging binary systems. The population characteristics of XRBs in nearby galaxies allow us to study how XRBs form in a variety of environments. The XRB evolution is quite different from isolated stars, and these sources are often divided into three distinct classes: high-mass XRBs (HMXBs) that have companion stars with masses $>8\,M_\odot$, low-mass XRBs (LMXBs) that have companion masses $<1\,M_\odot$, and intermediate-mass XRBs in between. Many of the so-called LMXBs most likely descended from the system where the donor star had an initial mass of 1.5–4.5 $M_\odot$ (e.g., Chen & Podsiadlowski 2016). The maximum lifetime of HMXBs is set by the nuclear burning time of an $8\,M_\odot$ star, which is about

3.3×10^8 yr (Verbunt & van den Heuvel 1995), whereas LMXBs have lifetimes of 10^{8-9} yr or more.

The Triangulum Galaxy, Messier 33 (M33), is an excellent galaxy for studying XRB populations. It is close enough (about 968 kpc away; Bonanos et al. 2006; U et al. 2009) to easily resolve individual X-ray sources but far enough away to be relatively small on the sky, allowing efficient coverage with the field of view of current X-ray instruments. Its relatively face-on orientation ($56° \pm 1°$; Zaritsky et al. 1989), relatively low Galactic foreground column density ($N_H = 6.0 \times 10^{20}$ cm^{-2}; Dickey & Lockman 1990), and active star formation make it an ideal laboratory for studying extragalactic HMXBs. The average star formation efficiency, the star formation rate (SFR) per unit gas mass, is $\sim 10^{-9}$ yr^{-1} (Elson et al. 2019). Williams et al. (2018) found a total SFR $= 0.17 \pm 0.06\,M_\odot$ yr^{-1} using the total infrared luminosity. From the infrared emission, Verley et al. (2007) derived an SFR for the inner disk equal to $0.2\,M_\odot$ yr^{-1}, consistent with the SFR obtained from the Hα emission. The total stellar mass in the M33 disk is estimated to be 3–$6 \times 10^9\,M_\odot$ (Corbelli 2003).

Table 1
NuStar X-Ray Observations for M33

Fields	(R.A., Decl.)	ObsID	Start Time (UT)	Exposure (s)
Field 1	(01:33:39, +30:38:30)	50310002001	2017-03-06 20:41:09	105,491
		50310002003	2017-07-23 13:21:09	101,775
Field 2	(01:34:17, +30:51:29)	50310003001	2017-03-09 05:01:09	105,965
		50310003003	2017-08-02 07:01:09	101,457
Field 3	(01:34:14, +30:30:50)	50310001004	2017-07-21 03:26:09	98,887
		50310001002	2017-03-04 10:56:09	108,139

Object M33 has a thin H I/stellar disk that extends out to a radius of ∼10 kpc (Corbelli & Schneider 1997).

The majority of sources in M33 are HMXBs (see, e.g., Tüllmann et al. 2011; Williams et al. 2015). Three HMXBs and a few other sources in M33 have been previously characterized as discussed below.

M33 X-8. This ultraluminous X-ray source (ULX) is coincident with the optical center of M33 (Dubus et al. 1997). Dubus et al. (1997) reported X-8 to have a periodicity of ∼106 days from 6 yr of ROSAT observations. Long et al. (2002) estimated the compact object to be an ∼10 $M_\odot$ black hole (BH), but super-Eddington accretion was not considered in that estimate. Krivonos et al. (2018) suggested that M33 X-8 is a stellar mass BH accreting at a high but subcritical accretion rate (a nearly Eddington rate) using two observations for M33 taken in 2017 March and July. It is possible, though, that the hard X-ray component is weak because the accretion columns are partially obscured by the inner thick disk. West et al. (2018) found that the 0.3–30 keV emission of X-8 is consistent with recent models of super-Eddington accretion onto either a BH or neutron star (NS) using nearly simultaneous NuSTAR and XMM-Newton observations.

M33 X-7. The mass of the BH in M33 X-7 (the first detected eclipsing BH–HMXB system; Pietsch et al. 2004) was constrained as $15.65 \pm 1.45\ M_\odot$ with a radial velocity curve based on Gemini North spectra and modeling (Orosz et al. 2007).

M33 X-6. Nikolaeva et al. (2018) suggested that this XRB might be a Z-source (i.e., an XRB with accretion near the Eddington limit onto a weakly magnetized NS; Maccarone et al. 2016) using data from NuSTAR and the Swift X-Ray Telescope (XRT).

Other sources of interest. A second eclipsing HMXB is located at R.A. $01^h32^m36^s.94$, decl. $+30°32'28''$ (J2000; Pietsch et al. 2009). The binary orbit was determined to be 1.732479 ± 0.000027 days with an eclipse half-angle of $30°.6$. Although pulsations were not detected in the X-ray flux, the hard X-ray spectrum may indicate that the compact object in the system is an NS (see, e.g., White et al. 1983). Also, Trudolyubov (2013) found a 285.4 s X-ray pulsar, XMMU J013359.5+303634, in M33.

In their Table 1, Tüllmann et al. (2011) summarized early X-ray surveys of M33, including the Einstein X-ray observatory (Long et al. 1981; Markert & Rallis 1983; Trinchieri et al. 1988), ROSAT (Schulman & Bregman 1995; Long et al. 1996; Haberl & Pietsch 2001), XMM-Newton (Pietsch et al. 2004; Misanovic et al. 2006), and Chandra (Grimm et al. 2005). In the Chandra ACIS survey of M33, Tüllmann et al. (2011) cataloged 662 X-ray sources, 183 of which had counterparts identified at other wavelengths allowing for their identification. Using a deep eight-field XMM-Newton mosaic of M33,

Williams et al. (2015) reported that only ∼50 of the 391 bright sources with luminosity $>3.6 \times 10^{35}$ erg s^{-1} belong to M33. Garofali et al. (2018) identified 55 candidate HMXBs in M33 using a combination of Chandra and the Hubble Space Telescope.

The broad energy band of NuSTAR allows us to distinguish compact object types based on discriminating spectral features. Within this harder band (4–25 keV), compact objects can be classified as NSs or BHs based on diagnostic diagrams (X-ray colors and luminosities; Wik et al. 2014b; Yukita et al. 2016; Lazzarini et al. 2018; Vulic et al. 2018). The hard X-ray emission from NSs is caused by the matter accretion process (di Salvo et al. 2004). The harder component from the accretion columns at the NS surface could have luminosities several times higher than the soft disk luminosity. Similarly, BHs emit soft X-rays from the disk (Mauche et al. 2004), although there is also hard X-ray flux from the corona (even if X-ray pulsars are typically even harder). Therefore, in a color–intensity diagram, pulsars have harder (bluer) colors, and BHs are softer. For the Z-source NSs, the hard X-rays are very likely from some "puffy" region with a disklike geometry. We also compare our results with the confirmed compact object types in the literature to demonstrate the validity of the technique.

In this paper, we use NuSTAR observations of M33 to classify 28 XRBs in M33 and constrain their accretion properties. Section 2 describes the data set. Section 3 discusses the reduction of the data and source detection technique. Section 4 details the resulting list, including count rates, hardness ratios, and source overlap with the previous XMM-Newton and Chandra catalog, and discusses the types of the sources. Section 6 summarizes the conclusions from discussions in Section 5.

2. Observations

NuSTAR has an angular resolution of 58″ half-power diameter and 18″ FWHM. Simultaneous observations from the dual telescopes A and B have a field of view over 12′ (Harrison et al. 2013; Kim et al. 2013). Therefore, in order to cover most of M33's optical extent, there were three pointings, conducted in 2017 March, July, and August. A total of six NuSTAR observations were completed with exposures of ∼100 ks each covering a part of M33, which are publicly available. The details of these observations are shown in Table 1. There are three fields of view (each with two separate epochs): field 1, 50310001002 and 50310001004; field 2, 50310002001 and 50310002003; and field 3, 50310003001 and 50310003003. We define field 1 as the middle field in Figure 1, while field 2 covers the northeast end of the galaxy and field 3 its southwest extent. The center of the field of view
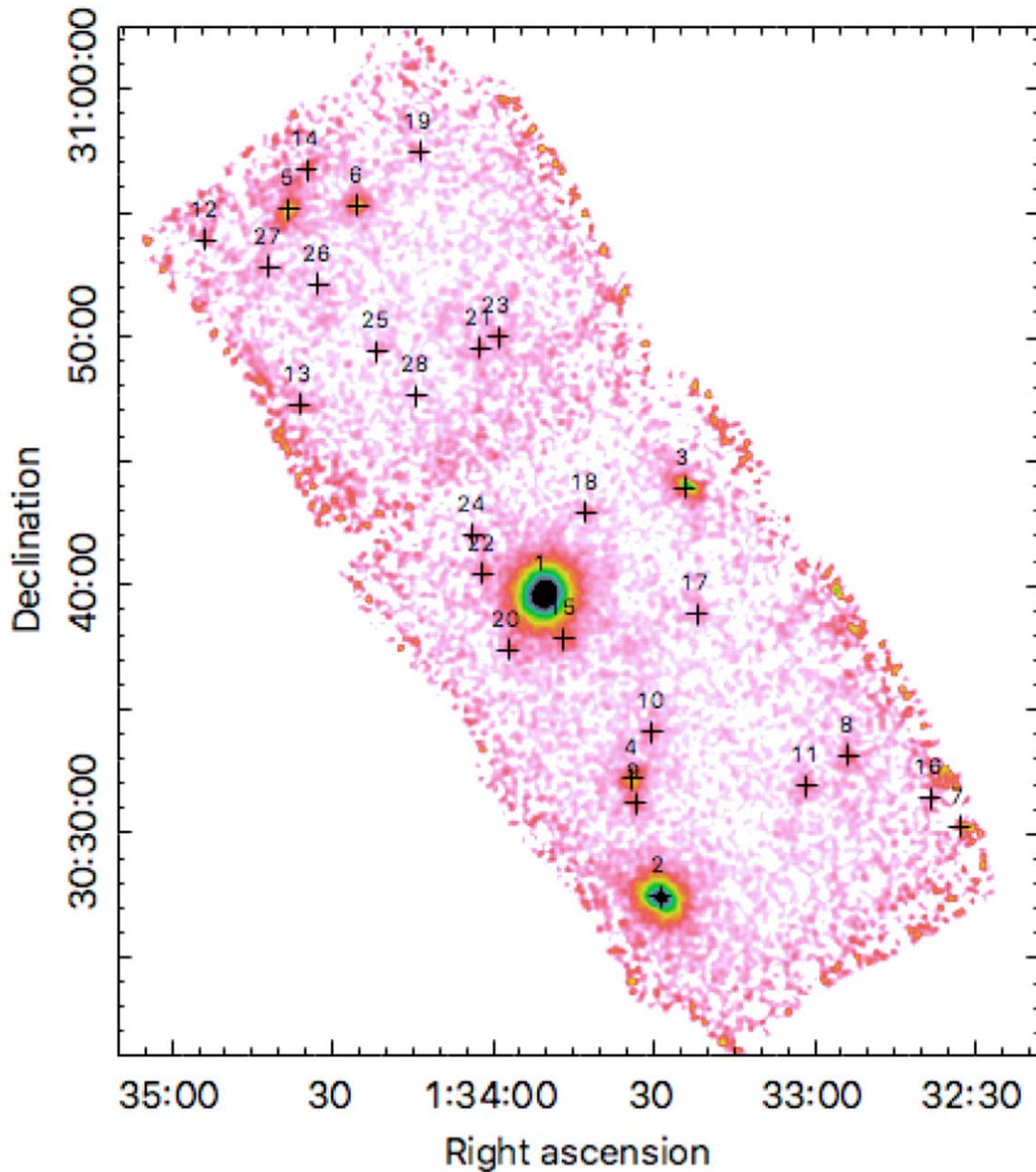
Figure 1. NuSTAR image of the central region in M33. The full smoothed NuSTAR mosaic contains six NuSTAR observations. We label the middle field as field 1, the upper left as field 2, and the bottom right as field 3; their details are shown in Table 1. The source numbers labeled are consistent with the numbers in Table 2.

of each observation is reported in Table 1, as well as the original exposure time before filtering.

3. Data Reduction

We used heasoft 6.22 and the associated CALDB files (version 075) for the data reduction. The event files are calibrated within 4–25 keV. The 4 keV was chosen as the lower limit of the energy band due to large calibration uncertainties below this limit, and the 25 keV upper limit was based on where many sources have reasonable signal. Above 25 keV, most sources are well below the noise level and undetected. The energy ranges are demonstrated by the channel numbers (CNs) in the commands of the analysis. The CN-to-energy (E) conversion is linear: $E = \mathrm{CN} \times 0.04\,\mathrm{keV} + 1.6\,\mathrm{keV}$ (lower

energy range of the bin).[13] For each field, we stack images from each epoch and instruments A and B together for our energy bands of interest.

From each instrument, the light curves were binned into 100 s intervals, and events were filtered to remove intervals of low and high background. The filtering options in the pipeline processing software (`nupipeline`) can effectively remove the high-background photon events but also periods when the background is not elevated. Therefore, we manually generate good time interval periods (GTIs) to maximize the time of good photon events. To do so, we exclude any regions with bright sources by manually generating and saving the excluded region files. We inspect light curves in the 50–160 keV band first, and we manually delete the high-background periods usually due to

---

[13] https://heasarc.gsfc.nasa.gov/docs/nustar/nustar_faq.html#pi_to_energy

passages of the spacecraft through the South Atlantic Anomaly. Here the 50–160 keV is only used to isolate high periods in NuSTAR's instrumental background. Using these updated GTIs as the input, the light curves are extracted within the 1.6–20 keV band, and any remaining high-background intervals contaminated by lower-energy solar flares are excluded by hand. Then we use nupipeline to process the cleaned event files with the final GTIs. The source background files are generated using the background characterization code nus-kybgd (Wik et al. 2014a). The code generates model background images based on the characterization of the background, which is necessary due to the spatial variation of the stray-light component of the background that dominates at these energies.

We use the nuexpomap command to generate exposure maps from the event files. To create an image in the 4–25 keV band, exposure maps are created at 10 keV for instruments A and B of each observation with the auxiliary file (i.e., attitude file). The locations of the six observations are aligned using the coordinates of known sources so that all of the source images, background images, and exposure maps can be mosaicked together. Then we do the background subtraction and exposure corrections for the mosaicked image. The final mosaic image is displayed in Figure 1 using the square root scale of the count rate in "hsv" color and an inverted color map.

We visually identified potential sources from the smoothed mosaicked image, which results in a complete initial candidate list. From experience with NuSTAR data, given its relatively large point-spread function (PSF) compared to the field of view and plate scale, the eye easily picks out source-like excesses down to 1σ. From this list, we detect 28 sources with significance larger than 3σ using the method described below. Some of them are known sources that have counterparts in XMM-Newton and/or Chandra. Some sources have more than one counterpart in Chandra. This final source list is shown in Table 2. The source numbers defined by us are shown in the column named "ID" and ordered by their measured 4–25 keV count rates. The coordinates are the center of the source extraction region (circular region with a radius of $7''$–$60''$, depending on the brightness of each source), from which we extract the source counts, as shown in Figure 2. The extraction radius is the uncertainty of the source coordinates in Table 2. The related source numbers, if there are any, in XMM-Newton (Williams et al. 2015) and Chandra (Tüllmann et al. 2011) are shown in the column "Previous ID." The labeled names shown in Figure 1 are from the column "ID." In order to extract the count rate and the corresponding significance of these sources/ source candidates, we applied the updated version of the IDL code based on the analysis from Wik et al. (2014b) with a refined PSF model used by Lazzarini et al. (2018) and Vulic et al. (2018). The source count rate is measured by fitting the image data to a model of the PSF generated for that bandpass and off-axis angle, allowing all corrections for vignetting, dead pixels or chip gaps, and energy dependence to be directly folded into the model. The count rates are also extracted in a soft energy band "S" within 4–6 keV, a medium band "M" within 6–12 keV, and a hard band "H" within 12–25 keV.

An example of the PSF-convolved point-source image, best-fitting model, and residuals for M33 X-8 is shown in Figure 2. For the top panels, the size of the model fit box is $3' \times 3'$, centered around M33 X-8. The smoothed data, model, and residual (data−model) images are shown in the left, middle,

and right panels, respectively. The data are represented by the black contours in the left panels and yellow in the right panels, while the white contours in all panels follow the underlying model image from the middle panels. With the estimated count rate of 0.1226 counts s^{-1} from SAO ds9 as the initial guess count rate for the model fits, the count rate for M33 X-8 is measured via PSF fitting to be $0.2055^{+0.0012}_{-0.0011}$. For the bottom panels, the size of the model fit box is $6' \times 5'$, which includes sources 15, 20, and 22 appearing as positive residuals. Although the PSF of X-8 has declined precipitously at the location of these sources, it can still contribute to an additional local "background" that needs to be accounted for to unbiasedly measure their count rates. When the rates of these sources are estimated, a smaller box size is used, but the model for X-8 is included (with no free parameters) so that this extra local background is included.

4. Results

4.1. NuSTAR Diagnostic Diagrams

We use NuSTAR hardness–intensity and color–color diagrams (for hardness–intensity and color–color diagrams generally, see, e.g., Maccarone & Coppi 2003; Done et al. 2007) to classify compact object types and accretion states (Figures 3 and 4). The X-ray spectral shapes are indicative of the accretion states, e.g., soft X-rays relating to the accretion disk and hard X-rays from nonthermal emission. This study is associated with and motivated by understanding the geometry and accretion mode of the compact objects. The spectral changes of the compact objects are linked to state transitions (e.g., Tananbaum et al. 1972).

The X-ray sources in M33 from NuSTAR were compared with Galactic BHs in different accretion states and with pulsars, as displayed in Figures 3 and 4. The Z/Atoll sources (i.e., nonmagnetized NSs) lie in a narrower range than BHs in the hardness–intensity and color–color diagrams, so we do not distinguish their accretion states. The S, M, and H bands are able to distinguish the accretion states of BH sources, which are more varied at NuSTAR energies. The Milky Way sources with well-categorized accretion states and compact object types were extracted from spectral model fits of thousands of RXTE PCA observations (as previously presented in, e.g., Wik et al. 2014b; Yukita et al. 2016; Vulic et al. 2018). In Figures 3 and 4, the Galactic BHs in different accretion states are plotted in blue (hard state), green (intermediate state), and red (soft state). The ULXs and accreting pulsars are shown with gray upside-down triangles and magenta squares, respectively. The ULX points are obtained from Vulic et al. (2018). Black stars represent the Z/Atoll sources based on spectral fits for Galactic LMXBs with RXTE and BeppoSAX observations. The Z/ Atoll sources group together but are separated from the magnetized pulsars. The luminosity axis is converted from the count-rate axis for the distance of M33.

The sources in M33 from NuSTAR observations are overplotted in black diamonds in Figures 3 and 4. Around[14] four sources (NuM33 12, 18, 21, and 27) are in the region of pulsars. About eight sources lie in the region of hard-state BH XRBs: NuM33 7, 11, 13, 16, 17, 19, 22, and 25. Source NuM33 13 is close to the boundary of the hard-state BH and pulsar and has counterparts in the XMM-Newton (No. 13) and

---

[14] Here we use "around" because the error bars on the hardnesses are large enough that the sources cannot be classified definitively.

Table 2
Sources in M33 Detected by NuSTAR X-Ray Observations

ID NuM33	R.A. (J2000)	Decl. (J2000)	Rate (4–25 keV) (10^{-3} counts s^{-1})	$\frac{M-S}{M+S}$	$\frac{H-M}{H+M}$	Previous ID XMM-Newton[a]	Previous ID Chandra[b]	Category NuSTAR
1	23.46105	30.660042	$205.5^{+1.2}_{-1.1}$	$-0.245^{+0.005}_{-0.005}$	$-0.786^{+0.005}_{-0.006}$	654	325, 318, 321	ULX (I, H, P)
2	23.3687	30.457672	$55.90^{+0.79}_{-0.75}$	$-0.019^{+0.012}_{-0.012}$	$-0.791^{+0.015}_{-0.014}$	1	180	I (Z, H)
3	23.350071	30.732233	$10.87^{+0.48}_{-0.45}$	$-0.071^{+0.034}_{-0.033}$	$-0.777^{+0.054}_{-0.056}$	9	156, 158	I
4	23.391317	30.536358	$7.840^{+0.346}_{-0.338}$	$-0.576^{+0.035}_{-0.037}$	<-0.890	3	225	S
5	23.660458	30.918378	$6.861^{+0.441}_{-0.412}$	$0.165^{+0.054}_{-0.056}$	$-0.527^{+0.07}_{-0.075}$	16	561	I (Z)
6	23.605917	30.921258	$5.934^{+0.625}_{-0.2}$	$0.048^{+0.054}_{-0.056}$	$-0.484^{+0.086}_{-0.063}$	14	492	I
7	23.135592	30.504333	$4.220^{+1.05}_{-1}$	$0.261^{+0.251}_{-0.225}$	$-0.337^{+0.26}_{-0.281}$			H
8	23.222604	30.552394	$3.131^{+0.422}_{-0.25}$	$0.129^{+0.088}_{-0.087}$	$-0.364^{+0.112}_{-0.1}$	6	37	I (H)
9	23.388396	30.520033	$3.110^{+0.319}_{-0.562}$	$-0.200^{+0.093}_{-0.1}$	$-0.329^{+0.126}_{-0.175}$	2	221	S
10	23.375804	30.567758	$2.624^{+0.327}_{-0.525}$	$0.058^{+0.11}_{-0.106}$	$-0.423^{+0.125}_{-0.2}$	4	195	I (H)
11	23.255617	30.531489	$2.346^{+0.365}_{-0.35}$	$0.220^{+0.094}_{-0.1}$	$-0.567^{+0.125}_{-0.15}$	5	64	H (I)
12	23.725033	30.897903	$2.104^{+0.481}_{-0.45}$	$0.449^{+0.271}_{-0.25}$	$0.058^{+0.188}_{-0.2}$			P
13	23.650704	30.787375	$2.058^{+0.347}_{-0.337}$	$0.304^{+0.147}_{-0.138}$	$-0.366^{+0.159}_{-0.175}$	13	553	H (P)
14	23.645767	30.945156	$1.971^{+0.492}_{-0.525}$	$0.050^{+0.313}_{-0.3}$	$-0.202^{+0.296}_{-0.325}$	17	546	I (H)
15	23.444554	30.630453	$1.970^{+0.257}_{-0.25}$	$-0.025^{+0.138}_{-0.125}$	$-0.393^{+0.156}_{-0.15}$	615	299	S (I)
16	23.158571	30.522978	$1.861^{+0.525}_{-0.5}$	$0.236^{+0.302}_{-0.262}$	$-0.144^{+0.265}_{-0.3}$	27		H
17	23.339908	30.647075	$1.721^{+0.234}_{-0.225}$	$0.327^{+0.164}_{-0.163}$	$-0.022^{+0.121}_{-0.125}$		141	H (P)
18	23.427292	30.715106	$1.629^{+0.234}_{-0.225}$	$0.318^{+0.14}_{-0.137}$	$-0.432^{+0.141}_{-0.15}$	10	281	P
19	23.557758	30.957517	$1.609^{+0.291}_{-0.3}$	$0.342^{+0.173}_{-0.175}$	$-0.220^{+0.173}_{-0.175}$			H
20	23.488104	30.623206	$1.485^{+0.234}_{-0.225}$	$0.124^{+0.148}_{-0.137}$	<-0.877	7	347	Z (H, I)
21	23.509762	30.825836	$1.425^{+0.29}_{-0.276}$	$0.377^{+0.225}_{-0.2}$	$-0.334^{+0.18}_{-0.188}$		396	P
22	23.507542	30.6741	$1.379^{+0.264}_{-0.275}$	$0.256^{+0.206}_{-0.187}$	$-0.491^{+0.219}_{-0.25}$			H (P, I)
23	23.496046	30.833381	$1.355^{+0.429}_{-0.175}$	$-0.126^{+0.183}_{-0.175}$	$-0.314^{+0.275}_{-0.262}$	12	365	S (I)
24	23.516083	30.700231	$1.158^{+0.306}_{-0.3}$	$0.153^{+0.218}_{-0.213}$	$-0.523^{+0.281}_{-0.35}$		398, 405	I
25	23.590408	30.822908	$1.129^{+0.2}_{-0.187}$	$0.138^{+0.132}_{-0.137}$	<-0.680			H (Z)
26	23.63725	30.868261	$1.055^{+0.235}_{-0.225}$	$-0.039^{+0.2}_{-0.2}$	$-0.155^{+0.232}_{-0.262}$			I
27	23.675458	30.879858	$1.023^{+0.306}_{-0.3}$	$0.378^{+0.344}_{-0.3}$	$-0.055^{+0.235}_{-0.262}$	15	577	P
28	23.559742	30.793358	$0.914^{+0.234}_{-0.225}$	$0.056^{+0.24}_{-0.25}$	$0.008^{+0.232}_{-0.263}$	11		I (H)

Notes. The total count rates with upper and lower limits are shown in the fourth column. The column $\frac{M-S}{M+S}$ is the hardness ratio between the medium and soft energy bands with the errors. The column $\frac{H-M}{H+M}$ is the hardness ratio between the hard and medium energy bands with error bars. We name each source in M33 detected by NuSTAR as "NuM33," where NuM33 1 is M33 X-8, NuM33 2 is M33 X-6, and NuM33 4 is M33 X-7. The last column is the source categories identified by NuSTAR: H (hard-state BH), I (intermediate-state BH), S (soft-state BH), P (pulsar), and Z (Z/Atoll sources). The classifications in parentheses show that the source is located in the overlapping regions or boundaries of two to three categories, and their identifications are uncertain.
[a] Williams et al. (2015).
[b] Tüllmann et al. (2011).

Chandra (No. 553) catalogs. Sources NuM33 20 and 25 are in the overlapping area of hard-state BH and Z/Atoll sources. The brightest source, M33 X-8 (NuM33 1), is a ULX. Approximately 10 and 4 sources fall within the intermediate- and soft-state BH region, respectively. There is some overlap between different populations, making classifications ambiguous (for example, the overlap between two categories of BHs and Z/Atoll sources). In some cases, the classifications are ambiguous due to the large error bars of the source hardness ratio and count rate.

The classifications of sources from the color–intensity diagram (Figure 3) are mostly consistent with the populations in the color–color diagram (Figure 4). Object M33 X-8 lies between the soft and intermediate BH areas but at higher luminosity (consistent with the spread in ULX $(M-S)/(M+S)$ colors). In Figure 4, NuM33 18 is in the pulsar region and close to the hard-state BH boundary, NuM33 21 aligns with the loci of the pulsars, and NuM33 22 is located in the overlapping region of the pulsar, hard-state BH, and intermediate-state BH. Source NuM33 18 has counterparts in the

XMM-Newton (No. 10) and Chandra (No. 281) catalogs, as shown in Table 2. Source NuM33 21 has a counterpart in the Chandra catalog (No. 396), and NuM33 22 is a new source detected by NuSTAR. In the color–color diagram (Figure 4), these sources are located between the pulsar and hard-state BH populations. Sources NuM33 7, 11, 13, 22, and 25 are hard-state BHs. Sources NuM33 20 and 25 could be either hard-state BH or Z/Atoll sources. Sources NuM33 2, 3, 5, and 24 are intermediate-state BHs. Sources NuM33 2 and 5 are in the overlapping area of intermediate-state BH and Z/Atoll sources. The uncertainty of the source classification is due to the error bars of the sources and the overlapping regions between different source categories. There are two to four sources in the soft-state BH population; NuM33 4 and 9 are soft-state BHs, and NuM33 15 and 23 are in the overlapping region of soft- and intermediate-state BHs. The remaining sources are potential intermediate BHs. The small number of sources in the soft state might be due to our selection criteria. We excluded the relatively faint sources that were not statistically significant (i.e., $<1\sigma$ or 3σ).
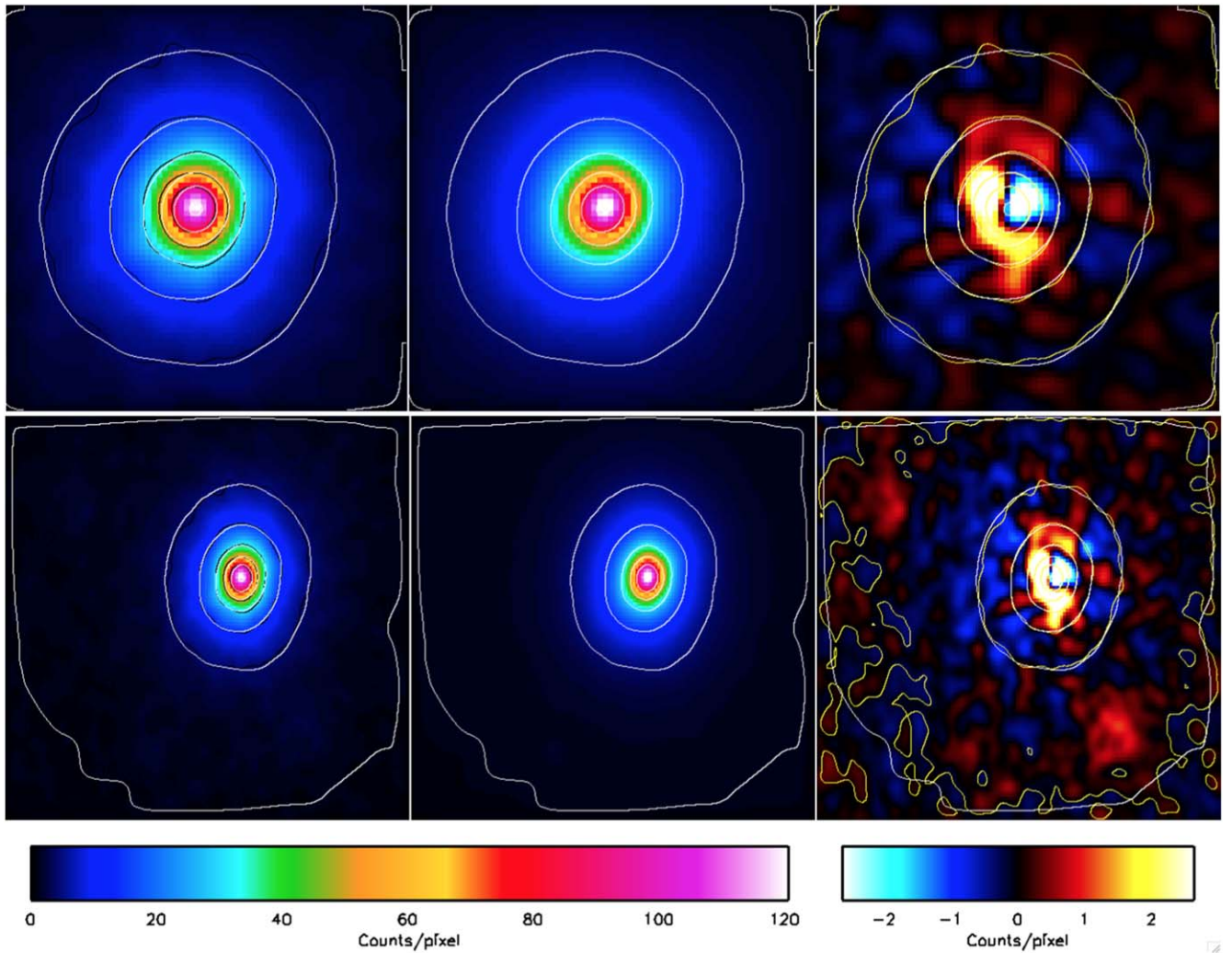
Figure 2. The PSF-calibrated point-source image fits for M33 X-8. The left panels display smoothed, background-subtracted counts data from both epochs. The middle panels show the best-fit model, and the white contours in all panels outline the smoothed model image. The right panels show the residual between data and model with a more restricted color scale. The yellow contours present the NuSTAR data. Both the yellow and white contours present identical intensities. For the top panels, the size of the model fit box is $3' \times 3'$, centered around M33 X-8. For the bottom panels, the size of the model fit box is $6' \times 5'$, which includes sources 15, 20, and 22, as shown in Figure 1.

4.2. Luminosity Function

The X-ray luminosity function (XLF) shows the histogram of the source X-ray luminosities. The shape of an LF is related to the metallicity and star formation history (Basu-Zych et al. 2016; Lehmer et al. 2021) of the host galaxy. Source count rates in 4–25 keV were converted to luminosities by assuming a power-law spectrum with photon index $\Gamma = 2$, which is broadly consistent with the average source spectrum. The source luminosity was calculated from count rates multiplied by a factor of 1.37×10^{40} erg counts^{-1}.

Figure 5 presents the LF for all sources with $>1\sigma$ significance in the hard energy band (12–25 keV) and $>3\sigma$ significance in the whole energy band (4–25 keV). One source (X-8) has a hard luminosity $>10^{38}$ erg s^{-1}, and seven bright sources' luminosities are higher than 10^{37} erg s^{-1}. The typical power-law shape of the XLF of point sources in nearby galaxies was reported by Grimm et al. (2002), Postnov (2003), and Mineo1 et al. (2014), as shown in the formula

$$\frac{dN}{dL_x} \propto \text{SFR} \times L_x^{-\alpha}, \tag{1}$$

where α is the slope of the differential distribution of a simple power law.

Is the XLF of M33 in the hard energy band different from the one in the soft band? The LF of the X-ray sources in M33 within the soft band (0.3–8.0 keV) in Grimm et al. (2005) is steep ($\sim 0.76 \pm 0.14$), likely due to the large number of background objects (Grimm et al. 2005). We used a power law to fit the LF of the M33 sources in the hard band, as shown by the red line (Figure 5). The power-law slope is 2 with a normalization of 105. The yellow line is the LF for active galactic nuclei (AGNs). Tüllmann et al. (2011) created cumulative LFs for the supernova remnants, XRBs, and unidentified sources in M33. The slope of their LF for XRBs is around 1.6, which is their expected value for a dominant HMXB population. Comparing to the "soft" XLF, it is also consistent with the deep XMM-Newton XLF from Williams et al. (2015), suggesting that the bright X-ray source population of M33 has a large fraction of HMXBs (a cumulative power-law index of 0.5, equivalent to a 1.5 differential index) when a background component is taken into account.
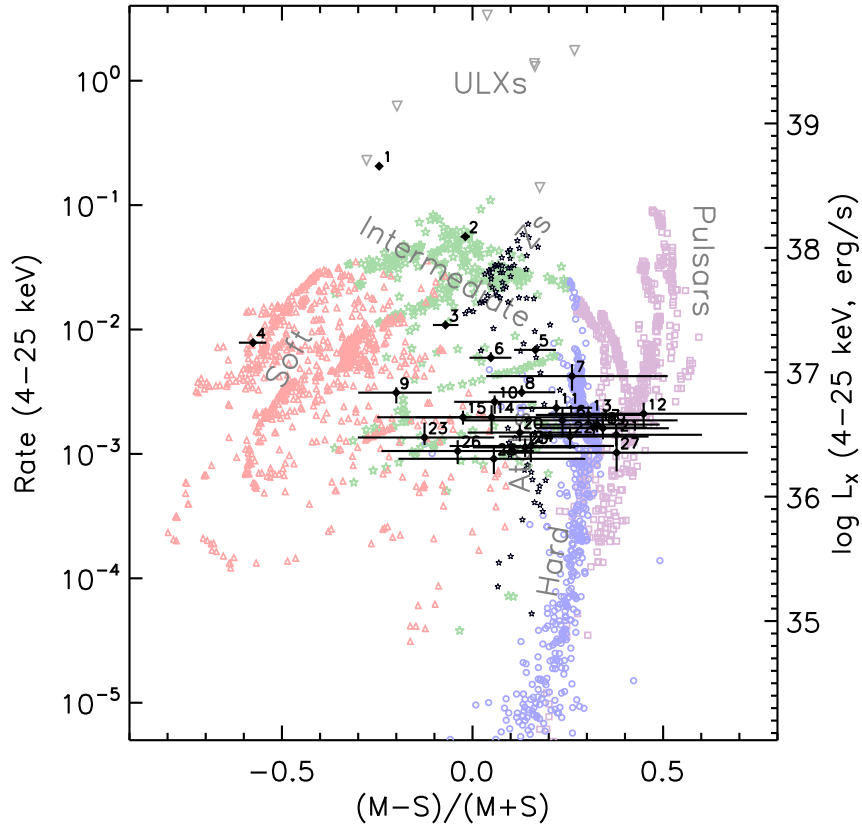
Figure 3. Hardness–intensity diagram for X-ray sources in M33 (black diamonds), pulsars (magenta squares), Z/Atoll sources (black stars), hard- (blue circles)/ intermediate- (green stars)/soft-state (red triangles) BH XRBs in the Milky Way, and ULXs (gray upside-down triangles) studied by NuSTAR. The hardness ratio is from $M = 6$–12 and $S = 4$–6 keV band count rates. The Y-axis is the total count rates within 4–25 keV. Our surveys thus far constrain the accretion-state distributions for luminous XRB populations in M33. These M33 observations constrain the distribution of accretion states for a low-luminosity HMXB-rich population. Note that NuM33 1 is M33 X-8, NuM33 2 is M33 X-6, and NuM33 4 is M33 X-7.

5. Discussion

5.1. Source Classification

As discussed in Table 2, NuM33 2 is M33 X-6, and NuM33 4 is M33 X-7. In the color–intensity diagram, X-6 overlaps with intermediate BH and Z-sources. In the color–color diagram, X-6 is located in the area of Z-sources and the edge of the hard-state BH. Therefore, we suggest that X-6 is likely a Z-source, an XRB with subcritical accretion onto a weakly magnetized NS, which is consistent with the results in Nikolaeva et al. (2018). Nikolaeva et al. (2018) described the source with a model of an optically and geometrically thick accretion disk and an additional hard component from Swift-XRT (0.3–10 keV) and NuSTAR (3–20 keV) data. Bogomazov (2014) used the "scenario machine" to study the evolution of M33 X-7, one of the most massive stellar mass BH candidates. Papadopoulos et al. (2021) studied the high-energy neutrino and γ-ray emission from the jets of the M33 X-7 microquasar. They performed detailed calculations for the cooling rates of various processes taking place in the hadronic jets of M33 X-7. The strong gravitational field of the compact object attracts the companion star's mass; an accretion disk formed in the equatorial region emits radiation and produces relativistic plasma jets all along the axis of rotation of the BH.

Most sources in Figures 3 and 4 overlap with intermediate- and hard-state BHs. In the color–color diagram, which has clearer separations between source types and accretion states,

some sources have much harder colors ($\frac{H-M}{H+M}$) than the Galactic sources. Their states are still not evident due to the scatter. The Z/Atoll sources are below the BH region and have hard spectra. Three sources overlap with hard-state BH and Z/Atoll sources. Based on their luminosities as shown in Figure 3, they were not in a ULX-like state at the time of these observations. Further observations from other wavelengths are needed in order to confirm the nature of the six new sources we found. If some source types in our diagnostic diagram are inconsistent with the literature, it may imply that this classification is not unique or needs to be better constrained. It could also mean that the classification method is galaxy-dependent, as this classification method is based on the source types in the Milky Way. We will also need other X-ray observations and optical follow-up to confirm the accuracy of the NuSTAR diagnostic for M33 compact object types.

5.2. M33 X-8

Object M33 X-8 is in the area of ULXs in the hardness–intensity diagram and located in the region of soft and intermediate BHs in the color–color diagram. Parola et al. (2015) reported the results of a Swift-XRT 6 yr monitoring campaign of X-8, which was persistently found to have a luminosity of a few 10^{39} erg s^{-1}, marking the faint end of the ULX LF. They described the average 0.5–10 keV spectrum with a thermal model, either in the form of a slim disk or as a
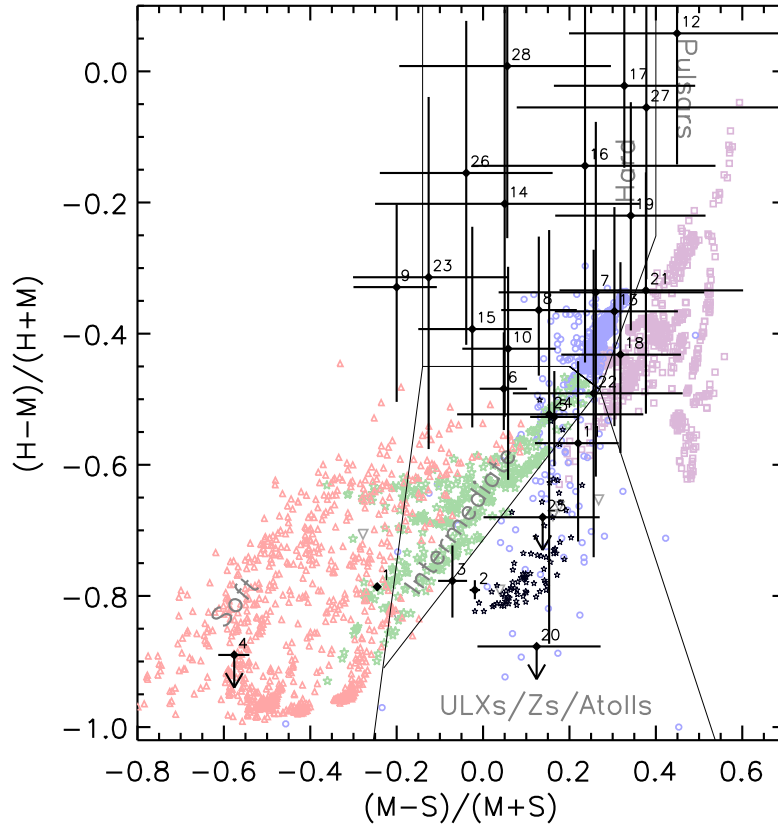
Figure 4. Color–color diagram. The black diamonds with error bars are the 28 sources in M33. Here NuM33 1 is M33 X-8, NuM33 2 is M33 X-6, and NuM33 4 is M33 X-7.

combination of a Comptonized corona and a standard accretion disk. West et al. (2018) presented nearly simultaneous NuSTAR and XMM-Newton observations of M33 X-8. They found that an additional high-energy Comptonization model is required, which rules out single advection-dominated disk and classical sub-Eddington models. West et al. (2018) found that the constraint is consistent with more recent models of super-Eddington accretion onto either a BH or NS, albeit with no clear preference. For the NS baseline model, the Comptonization component is modeled to be quite weak relative to the disk.

To confirm the nature of M33 X-8, we searched for pulsations in both NuSTAR epochs using Lomb–Scargle periodograms (the same method described in Yang et al. 2017a, 2019a). We found that a periodic signal was independently detected in both telescopes FPMA (769.42 ± 4.87 s) and FPMB (724.82 ± 5.22 s) with 99% significance during the first NuSTAR epoch (ObsID 50310002001). The significance of each periodicity was calculated from the number M of independent frequencies and Lomb–Scargle power P_X according to Press et al. (1992) and Yang et al. (2017a): $[1 - M \exp(-P_X)] \cdot 100\%$. The discrepancy between these candidate period values is not obviously explained by an observing window function effect. However, due to the inconsistency between period values in the two simultaneous observations and a lack of a physically compelling explanation for the discrepancy, we only claim that M33 X-8 remains a super-Eddington accreting pulsar candidate.

5.3. Comparison to Other Galaxies

Comparing to the other nearby galaxies as shown in Figure 2 of Vulic et al. (2018), M33 has a similar stellar mass as NGC 1313 and IC 342, its SFR is close to that of M31, and it has a much lower stellar mass than M31. For comparison, the LF of M31 and its LMXB-dominant population was modeled with a broken power law. The two indexes of their slopes are around 0.9 and 2.6. Fractionally, galaxies with higher values of SFR have more HMXBs. The BH fraction, $N_{\mathrm{BH}}/(N_{\mathrm{BH}} + N_{\mathrm{pulsar}})$, is about 0.85, since we are not sure if M33 X-8 is a pulsar, plus the source population overlap between BHs and Z/Atoll sources. If we do not take the different levels of detection sensitivities of different galaxies into account, this BH fraction is high based on Figure 5 of Vulic et al. (2018), which shows that a galaxy with a large SFR likely has a high fraction of BHs formed. Hard-state BHs are a large fraction of all identified accretion states of the samples in Vulic et al. (2018), as shown in their Table 4 and Figure 6. Object M33 hosts a large fraction of sources consistent with intermediate-state BHs. Accretion states depend more on the local environment, orbital parameters, and disk propagation. The total number of NSs and BHs is ~27, which is the largest population compared to the galaxies in Table 6 of Vulic et al. (2018). The number of BHs is also the largest. The number of NS and ULX populations is similar with most of the galaxies. Therefore, the XRB population of M33 can be considered a BH-dominated galaxy. The luminosity ranges of the hard-state BHs in M33 are between 10^{36} and 10^{38} erg s^{-1}. The maximum luminosity is consistent with the maximum luminosity of the
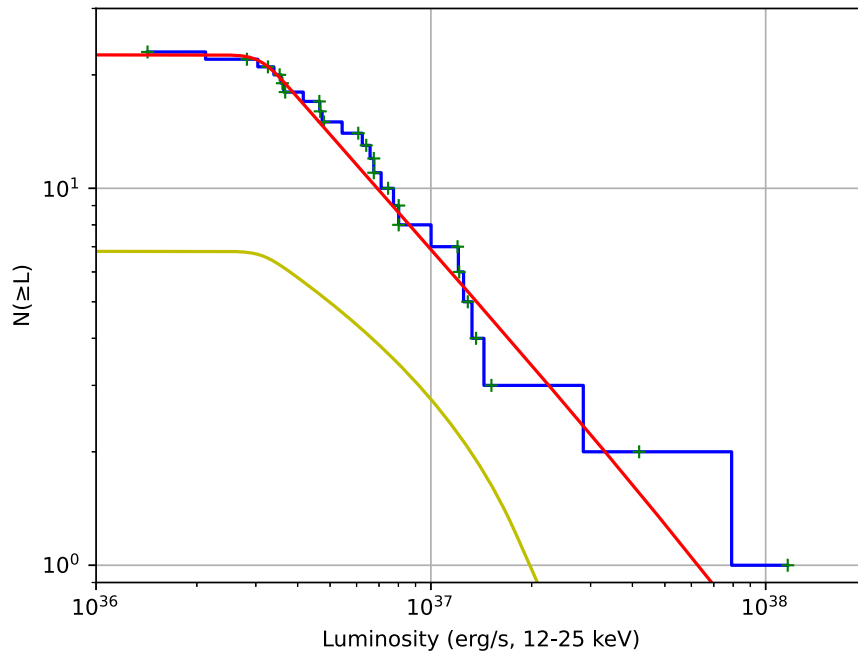
Figure 5. Cumulative LF of sources detected with $>1\sigma$ significance in the hard (12–25 keV) band (blue line). They are all detected with $>3\sigma$ significance in the 4–25 keV band. The red line is a power-law model whose slope is 2. The yellow line is the LF for AGNs.

hard-state BHs of the NuSTAR sample sources in Vulic et al. (2018).

The Small Magellanic Cloud (SMC) has a higher SFR ($\sim 0.3\,M_\odot\,\mathrm{yr}^{-1}$; Rezaei et al. 2014) than M33 and hosts the most X-ray pulsars (e.g., Yang et al. 2017b, 2018, 2019b). It is not surprising that the number of pulsars in M33 is small based on its lower SFR, especially since the population of SMC pulsars extends to much lower luminosities ($10^{31.2}$–$10^{38}\,\mathrm{erg\,s}^{-1}$) than we are sensitive to in M33 ($10^{36.2}$–$10^{36.8}\,\mathrm{erg\,s}^{-1}$). We can reach much lower luminosities in the SMC, so potentially, we can see many more faint pulsars there than we can in M33. This motivates deeper and more sensitive observations for M33 in the future.

The LF in the hard band in M33 shows a double peak and appears flat at the faint end due to the incompleteness. There is a drop, albeit with low significance, at $\sim 10^{37}\,\mathrm{erg\,s}^{-1}$. In M33, HMXBs and other young X-ray sources dominate instead of LMXBs, as is the case in M31, even though M33's total SFR is only about one-tenth that of the Milky Way. With a total stellar mass of $6.08 \pm 1.14 \times 10^{10}\,M_\odot$, the SFR for the Milky Way is $1.65 \pm 0.19\,M_\odot\,\mathrm{yr}^{-1}$ (Licquia & Newman 2015). The specific SFR of the Milky Way is $2.71 \pm 0.59 \times 10^{-11}\,\mathrm{yr}^{-1}$, smaller than M33. The Milky Way hosts slightly more LMXBs than HMXBs if a mass of $2.5\,M_\odot$ for the companion star is used as a boundary between LMXBs and HMXBs (Grimm et al. 2002).

Furthermore, the LF of the X-ray sources in M33 within the soft band in Figure 6 of Grimm et al. (2005) has a cumulative slope of 0.55 after subtraction of background AGNs. This slope is similar to the HMXB LF of the Milky Way ($\sim 0.64 \pm 0.15$) and the SMC. The shape of the HMXB XLF in the SMC is consistent with the $L^{-0.6}$ power law of the universal HMXB XLF (Shtykovskiy & Gilfanov 2005). The shape of the M33 XLF is similar to the total XLFs for all detected sources (in the broad energy band) from all galaxies in Vulic et al.'s (2018) sample.

6. Summary

We have classified 28 X-ray sources in M33 from six NuSTAR observations using diagnostic diagrams. Four sources lie in the parameter space occupied by X-ray pulsars, while 8, 10, and 4 sources lie in the parameter space occupied by BHs in the hard, intermediate, and soft states, respectively. Of the 28 sources, we have confirmed six new sources. The other 22 sources have XMM-Newton and/or Chandra counterparts. We claim that M33 is a BH-dominated galaxy based on the current number ratio of BHs and NSs detected. This is consistent with the conclusion in Vulic et al. (2018); most of their sample galaxies are BH-dominated, unlike M31 and NGC 4945, which are NS-dominated. Multiwavelength follow-up observations can help further confirm the properties of these M33 sources, especially the sources with large uncertainties on their count rates, in the overlapping areas of the compact object categories in the diagnostic diagrams, or with unconfirmed types (e.g., M33 X-8). The NuSTAR observations also provide a unique LF in the hard energy band. The shape of the LF shows that the X-ray sources in M33 are more consistent with an HMXB-dominated population over one made up of LMXBs based on comparison to older, and thus LMXB-dominated, sources in M31's bulge.

ORCID iDs

Jun Yang https://orcid.org/0000-0002-7584-4756
Daniel R. Wik https://orcid.org/0000-0001-9110-2245
Bret D. Lehmer https://orcid.org/0000-0003-2192-3296
Lacey A. West https://orcid.org/0000-0002-5523-4723
Benjamin F. Williams https://orcid.org/0000-0002-7502-0597
Andrew Ptak https://orcid.org/0000-0001-5655-1440

Neven Vulic ⓘ https://orcid.org/0000-0001-7855-8336
Dominic J. Walton ⓘ https://orcid.org/0000-0001-5819-3552
Kristen Garofali ⓘ https://orcid.org/0000-0002-9202-8689
Vallia Antoniou ⓘ https://orcid.org/0000-0001-7539-1593

References

Basu-Zych, A. R., Lehmer, B., Fragos, T., et al. 2016, ApJ, 818, 140
Bogomazov, A. I. 2014, ARep, 58, 126
Bonanos, A. Z., Stanek, K. Z., Kudritzki, R. P., et al. 2006, ApJ, 652, 313
Chen, W.-C., & Podsiadlowski, P. 2016, ApJ, 830, 131
Corbelli, E. 2003, MNRAS, 342, 199
Corbelli, E., & Schneider, S. E. 1997, ApJ, 479, 244
di Salvo, T., Santangelo, A., & Segreto, A. 2004, NuPhS, 132, 446
Dickey, J. M., & Lockman, F. J. 1990, ARA&A, 28, 215
Done, C., Gierliński, M., & Kubota, A. 2007, A&ARv, 15, 1
Dubus, G., Charles, P. A., Long, K. S., & Hakala, P. J. 1997, ApJL, 490, L47
Elson, E. C., Kam, S. Z., Chemin, L., Carignan, C., & Jarrett, T. H. 2019, MNRAS, 931, 483
Garofali, K., Williams, B. F., Hillis, T., et al. 2018, MNRAS, 479, 3526
Grimm, H.-J., Gilfanov, M. R., & Sunyaev, R. A. 2002, A&A, 391, 923
Grimm, H.-J., McDowell, J., Zezas, A., Kim, D.-W., & Fabbiano, G. 2005, ApJS, 161, 271
Haberl, F., & Pietsch, W. 2001, A&A, 373, 438
Harrison, F. A., Craig, W. W., Christensen, F. E., et al. 2013, ApJ, 770, 103
Kim, Y., Willis, J., Dodd, S., et al. 2013, in IEEE Aerospace Conference (Piscataway, NJ: IEEE), 122
Krivonos, R., Sazonov, S., Tsygankov, S. S., & Poutanen, J. 2018, MNRAS, 480, 2357
Lazzarini, M., Hornschemeier, A. E., Williams, B. F., et al. 2018, ApJ, 862, 28
Lehmer, B. D., Eufrasio, R. T., & Basu-Zych, A. 2021, ApJ, 907, 17L
Licquia, T. C., & Newman, J. A. 2015, ApJ, 806, 96
Long, K. S., Charles, P. A., Blair, W. P., & Gordon, S. M. 1996, ApJ, 466, 750
Long, K. S., Charles, P. A., & Dubus, G. 2002, ApJ, 569, 204
Long, K. S., Dodorico, S., Charles, P. A., & Dopita, M. A. 1981, ApJL, 246, L61
Maccarone, T. J., & Coppi, P. S. 2003, MNRAS, 338, 189
Maccarone, T. J., Yukita, M., Hornschemeier, A., et al. 2016, MNRAS, 458, 3633
Markert, T. H., & Rallis, A. D. 1983, ApJ, 275, 571
Mauche, C. W., Liedahl, D. A., Mathiesen, B. F., Jimenez-Garate, M. A., & Raymond, J. C. 2004, ApJ, 606, 168

Mineo1, S., Rappaport, S., Levine, A., et al. 2014, ApJ, 797, 91
Misanovic, Z., Pietsch, W., Haberl, F., et al. 2006, A&A, 448, 1247
Nikolaeva, S. M., Krivonos, R. A., & Sazonov, S. Y. 2018, AstL, 44, 593
Orosz, J. A., McClintock, J. E., Narayan, R., et al. 2007, Natur, 449, 872
Papadopoulos, D. A., Papavasileiou, V. Th., & Kosmas, T. S. 2021, JPhCS, 1730, 012137
Parola, L. L., D'Ai, A., Cusumano, G., & Mineo, T. 2015, A&A, 580, A71
Pietsch, W., Haberl, F., Gaetz, T. J., et al. 2009, ApJ, 694, 449
Pietsch, W., Misanovic, Z., Haberl, F., et al. 2004, A&A, 426, 11
Pietsch, W., Mochejska, B. J., Misanovic, Z., et al. 2004, A&A, 413, 879
Postnov, K. A. 2003, AstL, 29, 372
Press, W. H., Teukolsky, S. A., Vetterling, W. T., & Flannery, B. P. 1992, Numerical Recipes in FORTRAN. The Art of Scientific Computing (Cambridge: Cambridge Univ. Press)
Rezaei, k. S., Javadi, A., Khosroshahi, H., & Loon, J. 2014, MNRAS, 445, 2214
Schulman, E., & Bregman, J. N. 1995, ApJ, 441, 568
Shtykovskiy, P., & Gilfanov, M. 2005, MNRAS, 362, 879
Tananbaum, H., Gursky, H., Kellogg, E., Giacconi, R., & Jones, C. 1972, ApJL, 177, L5
Trinchieri, G., Fabbiano, G., & Peres, G. 1988, ApJ, 325, 531
Trudolyubov, S. P. 2013, MNRAS, 435, 3326
Tüllmann, R., Gaetz, T. J., Plucinsky, P. P., et al. 2011, ApJS, 193, 31
U, V., Urbaneja, M. A., Kudritzki, R.-P., et al. 2009, ApJ, 704, 1120
Verbunt, F., & van den Heuvel, E. P. J. 1995, in X-Ray Binaries, ed. W. H. G. Lewin, J. van Paradijs, & E. P. J. van den Heuvel (Cambridge: Cambridge University Press), 457
Verley, S., Hunt, L. K., Corbelli, E., & Giovanardi, C. 2007, A&A, 476, 1161
Vulic, N., Hornschemeier, A. E., Wik, D. R., et al. 2018, ApJ, 864, 150
West, L. A., Lehmer, B. D., Wik, D., et al. 2018, ApJ, 869, 111
White, N. E., Swank, J. H., & Holt, S. S. 1983, ApJ, 270, 711
Wik, D. R., Hornstrup, A., Molendi, S., et al. 2014a, ApJ, 792, 48
Wik, D. R., Lehmer, B. D., Hornschemeier, A. E., et al. 2014b, ApJ, 797, 79
Williams, B. F., Wold, B., Haberl, F., et al. 2015, ApJS, 218, 9
Williams, T. G., Gear, W. K., & Smith, M. W. L. 2018, MNRAS, 479, 297
Yang, J., Laycock, S. G. T., Christodoulou, D. M., et al. 2017a, ApJ, 839, 119
Yang, J., Laycock, S. G. T., Drake, J. J., et al. 2017b, AN, 338, 220
Yang, J., Laycock, S. G. T., & Wik, D. R. 2019a, AN, 340, 62
Yang, J., Wik, D. R., Zezas, A., et al. 2019b, AN, 340, 46
Yang, J., Zezas, A., Coe, M. J., et al. 2018, MNRAS, 479, L1
Yukita, M., Hornschemeier, A. E., Lehmer, B. D., et al. 2016, ApJ, 824, 107
Zaritsky, D., Elston, R., & Hill, J. M. 1989, AJ, 97, 97